IRANIAN JOURNAL OF CATALYSIS

IJC
Iranian Journal of Catalysis

The Study of Photocatalytic Degradation Mechanism under Visible Light Irradiation on BiOBr/Ag Nanocomposite

Marzieh Yaghoubi-berijani[a], Bahram Bahramian*[a] Solmaz Zargari[b]

a) Faculty of Chemistry, Shahrood University of Technology, Shahrood, 3619995161-316, Iran.
b) University of Applied Science and Technology (UAST), Ghand Center, Karaj, Iran.

ABSTRACT

Due to the pollution of dyeing and textile industry wastewaters in different colors and the need to remove these pollutants from the wastewaters, it is necessary to study and develop effective and efficient technology solutions required. To remove dye from aqueous solutions, photodegradation is employed as an effectively simple way. Thus, the BiOBr photocatalyst was chemically made by synthesis using a facile method. To enhance its photocatalytic activity, the synthesized BiOBr nanoplates were then functionalized with Ag NPs forming the modified BiOBr/Ag photocatalyst. The BiOBr/Ag nanocomposite was synthesized with different percentages of Ag to determine its optimized percentage in the photocatalytic process. The characterization techniques of PL, DRS, XRD, EDX, SEM, FT-IR, and Raman were used to confirm the prepared samples. The power-down white light lamp was used in the photocatalytic process, which showed good degradation. The photocatalytic activity of prepared BiOBr/Ag was investigated by the degradation of the 2,4-dichlorophenol, methyl orange, and rhodamine B. The effective separation and inhibited recombination of photo-generated electron-hole pairs resulted from the high photocatalytic activity.

Keywords: *Nanocomposite; Bismuth oxybromide; BiOBr/Ag; Photocatalytic process.*

1. Introduction

Among different types of wastewaters, dyeing wastewater deserves considerable attention. Due to the pollution of dyeing and textile industry wastewaters in different colors, large amounts of dyes are released into the environment. There are two major types of dye: natural and synthetic. Synthetic dyes are made in a laboratory, particularly used in the textile industry, and have gradually replaced natural dyes. It is necessary to study and provide effective and efficient technology with low investment and exploitation expenses [1, 2].

Efficient techniques are required for serious organic pollutants to eliminate their harmful effects. One of the key approaches to preventing harmful organic pollution is chemical degradation. To remove organic contaminants, the semi-conductor photocatalysis technique is quick and low price, which is environmentally friendly [3-5].

Lately, a series of ternary oxide semiconductors, such as bismuth oxyhalides BiOXs (BiOCl, BiOBr, and BiOI), has received much consideration owing to their excellent photocatalytic efficiency [6]. BiOXs are inexpensive photocatalysts that are non-toxic and non-harmful to the environment. Therefore, BiOXs have emerged as inexpensive semi-conductors with promising applications in the manufacture of photoelectrochemical cells and the photocatalytic degradation of dangerous pollutants [7, 8]. Among BiOXs, BiOBr has recently been found to be the most ideal compound having appropriate band gap (2.8 eV), low toxicity, excellent photocatalytic ability, and great chemical stability for the photocatalytic process. Therefore, many efforts have been dedicated to developing the synthesis of BiOBr nanostructures, where a high ratio of surface-to-volume is ready to increase the photocatalytic activity [9].

---

*Corresponding author.
E-mail address: *bahramian.b@shahroodut.ac.ir*
(B. Bahramian)

The reaction process of BiOX preparation is provided in Eq. (**1**) and (**2**) [10]:

$$Bi(NO_3)_3 + H_2O \rightarrow BiONO_3 + 2HNO_3 \quad \textbf{(1)}$$

$$BiONO_3 + KX \rightarrow BiOX + KNO_3 \quad \textbf{(2)}$$

Having diverse applications and various physio-chemical features, nanoparticles (NPs) [11] have recently attracted considerable attention. To boost BiOBr photocatalytic activity, noble metals like Ag, Au, Pt, and Pd have been incorporated into its surface because these metals can act as electron traps [12]. Moreover, the noble metal NPs could be coupled with a semi-conductor to improve its photocatalytic characteristics considerably due to the energy level matched between the noble metal NPs and the semi-conductor as well as the Surface Plasmon Resonance (SPR) of these NPs [13-15]. The silver nanoparticles of Ag NPs are increasingly used in different fields, including food, industry, health, and medical care because of their unique physical and chemical characteristics including optical and biological property as well as electrical conductivity [16-18]. The immobilization of Ag NPs on the semi-conductor photocatalysts can improve their photocatalytic activity, as one of the important research goals in the photocatalysis area [19, 20].

In this paper, a simple method was successfully used for the fabrication of BiOX/metal NPs system. The nanocomposite was synthesized based on BiOBr/Ag, using a simple sample for separation of photo-degradation loads and electron transport. Moreover, the photocatalytic activity of the compositions was studied for the photo-degradation of pollutants and a good photocatalytic activity was exhibited under the irradiation of (low-power, 5-W) LED. The photocatalytic activity mechanism was also investigated using several scavengers to reveal the effect of holes on the photocatalytic process.

2. Experimental

2. 1. Instrumentation and Materials

By the use of Zeiss ΣIGMA|VP (Germany) FE-SEM/EDX, Field Emission-Scanning Electron Microscope (FE-SEM), and Energy-Dispersive X-ray (EDX) spectroscopy were respectively employed to test the morphology and the elemental composition of the samples. Making use of Shimadzu MPC-2200 spectrophotometer, UV-visible Diffusive Reflectance Spectra (DRS) was recorded. Rayleigh spectrophotometer (China) was also used to measure Fourier transform infrared spectroscopy (FT-IR). By means of D8-Advanced Bruker and Cu Kα radiation (λ= 0.15406 nm), the crystalline phase structure of the samples was obtained. Shimadzu RF-6000 Spectro fluorophotometer was utilized to measure photoluminescence spectra (PL). On double-beam Perkin-Elmer (America, lambda 360) and uRaman-532-Ci Raman (Avantes Company, Netherland) spectrometers, UV-visible, and Raman spectra were respectively determined. The photocatalytic activity was evaluated for the visible irradiation of the power down white light (5-W white LED, IF: 300 MA, VF: 15–18 V, TC: 600–8500 K). With no further purification, the potassium bromide, bismuth (III) nitrate, silver nitrate (AgNO₃), nitric acid, sodium borohydride, sodium acetate, ammonium oxalate (NH₄OX), and tert-butanol (Tert-BuOH) by Merk Company were used.

2.2. Synthesis of BiOBr and BiOBr/Ag nanocomposites

The BiOBr nanoplates were prepared according to previous work [21]. To provide solution A, $Bi(NO_3)_3$ catalyst was uniformly dispersed in 15 ml HNO₃. To make solution B, 0.02 mol CH₃COONa and 0.01 mol KBr were dissolved in 100ml distilled water. Solution A was rapidly poured into solution B yielding a white mixture, then stirred for 12 hours to complete the reaction.

To prepare the BiOBr/Ag nanocomposite, an aqueous solution of BiOBr (0.2 g) was mixed with an aqueous solution of AgNO₃ (0.1 M). Then 10 ml freshly prepared NaBH₄ was added to the mixture dropwise, stirring for about 5 hours. Eventually, the resulting precipitate was centrifuged, washed in distilled water, and dried in the oven. The concentrations of Ag NPs in different samples are tabulated in **Table 1**.

Table 1. Concentration of Ag NPs in various samples

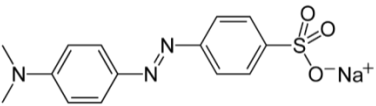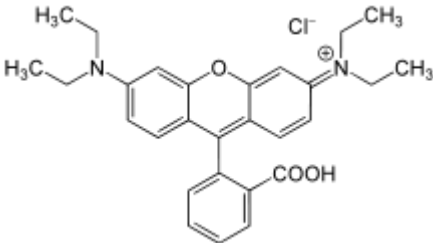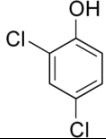| Sample	BiOBr/Ag (a)	BiOBr/Ag (b)	BiOBr/Ag (c)
Concentration of Ag (mol/L)	0.05	0.1	0.1
BiOBr (g)	0.2	0.1	0.2

2.3. RhB, MO, and DCP Photodegradation

The process of photodegradation was studied for the colored contaminants of methyl orange (MO, pH=3),

2,4-Dichlorophenol (2,4-DCP), and Rhodamine B (RhB) (**Table 2**) at a concentration of 10 g L^{-1} to evaluate photocatalytic activity of the prepared BiOBr and BiOBr/Ag in the presence of optimized amount of the photocatalysts (0.03 g) under the visible 5-W white light LED irradiation. Stirring about half an hour in the darkness, the mixture achieved an equilibrium between adsorption and desorption rates of the organic pollutant and the sample. About 0.003 mL mixture was then centrifuged to record the changes in the adsorption of the organic pollutant at specific intervals of one hour under the irradiation of visible light.

Table 2. Physico-chemical characteristics of the organic pollutants.

| Organic pollutant	Chemical formula	Chemical structure	Molar mass (g mol^{-1})
MO	$C_{14}H_{14}N_3NaO_3S$		327.33
RhB	$C_{28}H_{31}ClN_2O_3$		479.02
DCP	$C_6H_4Cl_2O$		163.00

3. Results and Discussion

3. 1. 1. FT-IR Analysis

Fig. 1 illustrates the FT-IR spectra representing the BiOBr and BiOBr/Ag (c) chemical structures. As expected, the vibration peaks at about 511 cm^{-1} and 513 cm^{-1} for the Bi-O bond were observed in the corresponding spectra of BiOBr and BiOBr/Ag (c), indicative of the BiOBr existence [21, 22]. In addition, the intensity of the characteristic band in the spectrum of BiOBr for the metal-oxygen bond (Bi-O) became weaker for the BiOBr/Ag nanocomposite. This result, i.e. the obvious interaction between Ag and the BiOBr nanoplates, proposes a successful hybridization between these two components [23].

3.1.2. UV–visible DRS

Enhanced adsorption of the visible light leads to the higher generation of photogenerated charge carriers and, in turn, improves the semi-conductor photocatalytic efficiency. **Fig. 2** represents the UV–visible DRS spectroscopy for the BiOBr nanoplates and the BiOBr/Ag (a, b, c) nanocomposites. The samples exhibited different absorptions in the visible light zone. The band gap for the semi-conductors was deduced from plotting out the curve of $(\alpha h\upsilon)^2$ against photon energy ($h\upsilon$) intersected with the linear portion extrapolation. The absorption ratio and the light frequency are respectively shown by α and υ, and h is taken as the Planck's constant. According to Fig. 2, there is a peak at 440 nm in the pure BiOBr spectrum, which can be ascribed to the absorption property for a band gap of 2.8 eV. The deposition of Ag in the BiOBr makes an obvious shift from the absorption edge onto the long wavelength direction. The absorption of BiOBr/Ag, in comparison with pure BiOBr, is developed to the visible light zone, which can be due to the presence of Ag. After loading the Ag NPs, a peak of surface plasmon resonance (SPR) emerges at 460 nm in the BiOBr/Ag (c) absorption spectrum. The strong absorption of Ag can provide a grounding for the absorption of as-prepared BiOBr/Ag nanocomposite in the visible light zone. The number of photo-generated holes and electrons is increased by increasing light absorption, leading to some improvements in the photocatalytic reaction and performance [24].
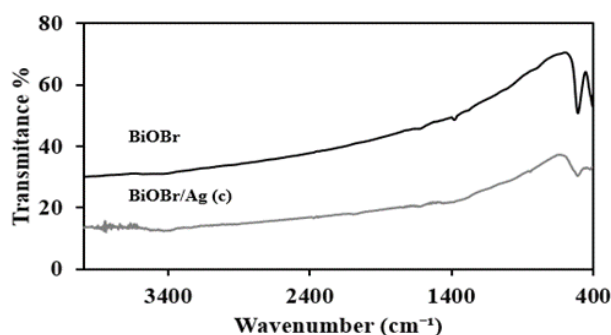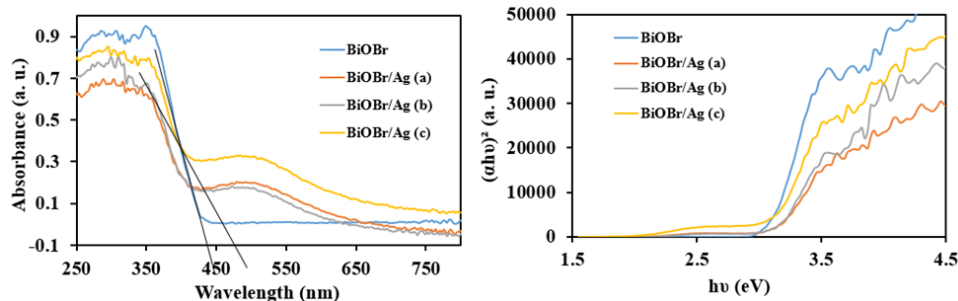
Fig. 1. FT-IR spectra for BiOBr and BiOBr/Ag (c) nanocomposite.

The absorption edges (λg) and estimated band gap energies (Eg) for the synthesized compounds can be seen in **Table 3**. The results reveal that the BiOBr/Ag (c) nanocomposite has efficiently powered the light-harvesting ability of this compound. Similarly, the CB and VB edges of BiOBr are obtained by the following empirical formulas **(3)** and **(4)** [25, 26]:

$$E_{VB} = X - E_e + 0.5E_g \qquad (3)$$

$$E_{CB} = E_{VB} - E_g \qquad (4)$$

where E_{CB} and E_{VB} respectively denote the conduction band (CB) and the valence band (VB) potentials, X implies the BiOBr absolute electronegativity i.e. the mean electronegativity of the constituent atoms. The E_g and E^e respectively represent the energy of BiOBr band gap and the energy of free electrons (ca. 4.5eV) on hydrogen scale. The values of E_{CB}, E_{VB}, and X for BiOBr are equal to 0.278 eV, 3.078 eV, and 6.178 eV, respectively.

Table 3. Absorption edge (λg) and estimated band gap energy (Eg) values for the photocatalysts.

| Sample	λg (nm)	Eg (eV)
BiOBr	440	2.8
BiOBr/Ag (a)	430	2.9
BiOBr/Ag (b)	430	2.9
BiOBr/Ag (c)	460	2.7

Fig. 2. UV–visible diffusive reflectance spectra for the photocatalysts.

3.1.3. XRD Analysis

Making use of XDR analysis, the structure of the crystalline phase was studied for the samples. **Fig. 3a** demonstrates the XRD patterns for the catalyst BiOBr and the composite catalyst BiOBr/Ag (c). The reflection peaks appeared at 2θ= 57.08°, 50.52°,46.16°, 39.2°, 31.92°,31.56°,25.08°,21.8°, and 10.76° corresponding to the planes (212), (014), (020), (112), (110), (012), (001), (002), and (001) respectively [21]. The XRD data show sharp and strong peaks for BiOBr, suggestive of its being well-crystalized. The XRD result for BiOBr/Ag (c) effectively confirms the existence of Ag in this compound.

Considering the strain and crystallite contribution to the peak broadening as well as Williamson–Hall analysis, the BiOBr crystallite size has been calculated from Eq.**(5)** [27, 28].

$$\beta \cos \theta = C \sin\theta + K\lambda/L \qquad (5)$$

where X-ray wavelength and the average crystallite size are respectively represented by λ and L. the shape coefficient k is taken to be 0.9 for the reciprocal lattice point, and θ identifies the crystalline phase peak position. Fig. 3b shows plots of $\beta \cos \theta$ versus $\sin \theta$ (W–H plot) for the BiOBr nanoplates synthesized. It is possible to observe that the straight line intercepts all points, indicating a homogeneous crystallite size distribution. According to the results, the crystallite size of the BiOBr nanoplate is 34 nm.

The conventionally used Debye-Scherrer equation will yield a moderate crystallite size, neglecting both form and the strain state. We have calculated the crystallite size of BiOBr NPs to be 33 nm by the Debye-Scherrer formula **(Eq.6).**

$$L = K\lambda/\beta \cos\theta \qquad (6)$$
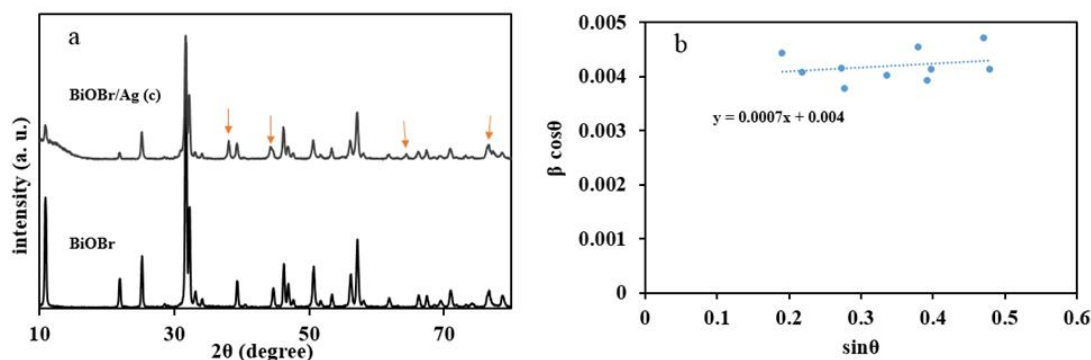
Fig. 3. a) Comparison of the XRD patterns between BiOBr and BiOBr/Ag (c) nanocomposite and b) Williamson–Hall plot of the BiOBr nanoplates.

3.1.4. FE-SEM Images

The morphology of the samples was evaluated using FE-SEM. The SEM and EDX photographs for the samples are presented in **Fig. 4.** As shown in Fig. 4a, BiOBr consists of irregular nanoplate structures and Figs. 4b and 4c show BiOBr/Ag (c) with a width ranging from 20 nm to 50 nm. Some small particles can be observed over the smooth surface, where Ag NPs display a good distribution of uniform particle sizes on the surface of BiOBr nanoplates. As illustrated in Fig. 4c, the thickness of the BiOBr nanoplates became lower. It was revealed that the BiOBr nanoplates included a smooth surface had a rough surface after the modification of Ag NPs [20].

Moreover, the elemental compositions of pure BiOBr and BiOBr/Ag (c) were analyzed using EDX spectroscopy. The peaks associated with Br, O, and Bi can be observed in **Fig. 5a**. This figure presents the EDX spectrum for the BiOBr/Ag nanocomposite, in which a weak Ag peak is observed because of its little amount. Once again, the presence of Ag in the BiOBr/Ag (c) nanocomposite was supported. Based on theoretical calculations, the amount of Ag in the BiOBr/Ag nanocomposite obtained was 13.5%, which is 1% different from the EDS results (12.5%).

The Ag NPs distributions were evaluated by histogram analysis. The histogram derived from SEM is shown in **Fig. 5b.** In the histogram, each column corresponds data to the ranges, and the higher the column, the wider the range of data. As can be seen, the size distribution of Ag NPs is in the range 15-30 nm, and the highest population is associated with 23 nm.
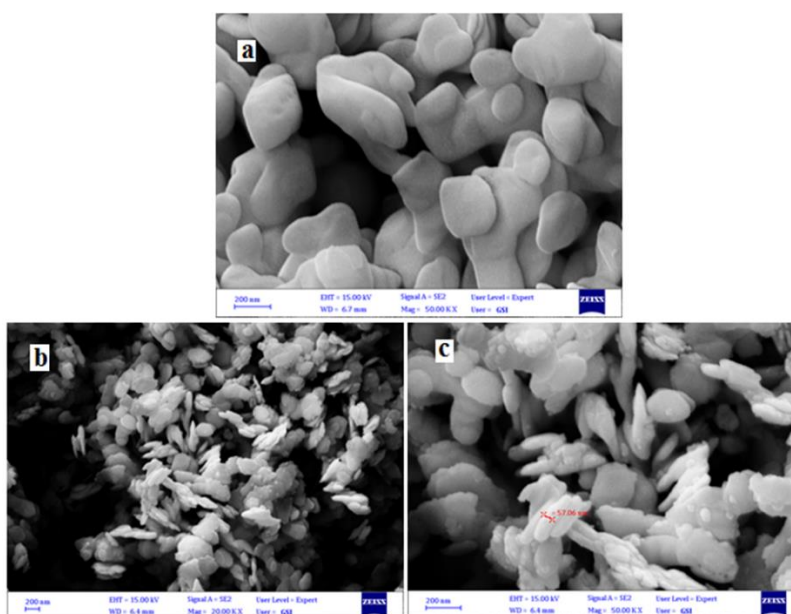
**Fig.4.** SEM images for a) BiOBr, b) and c) BiOBr/Ag (c) nanocomposite.
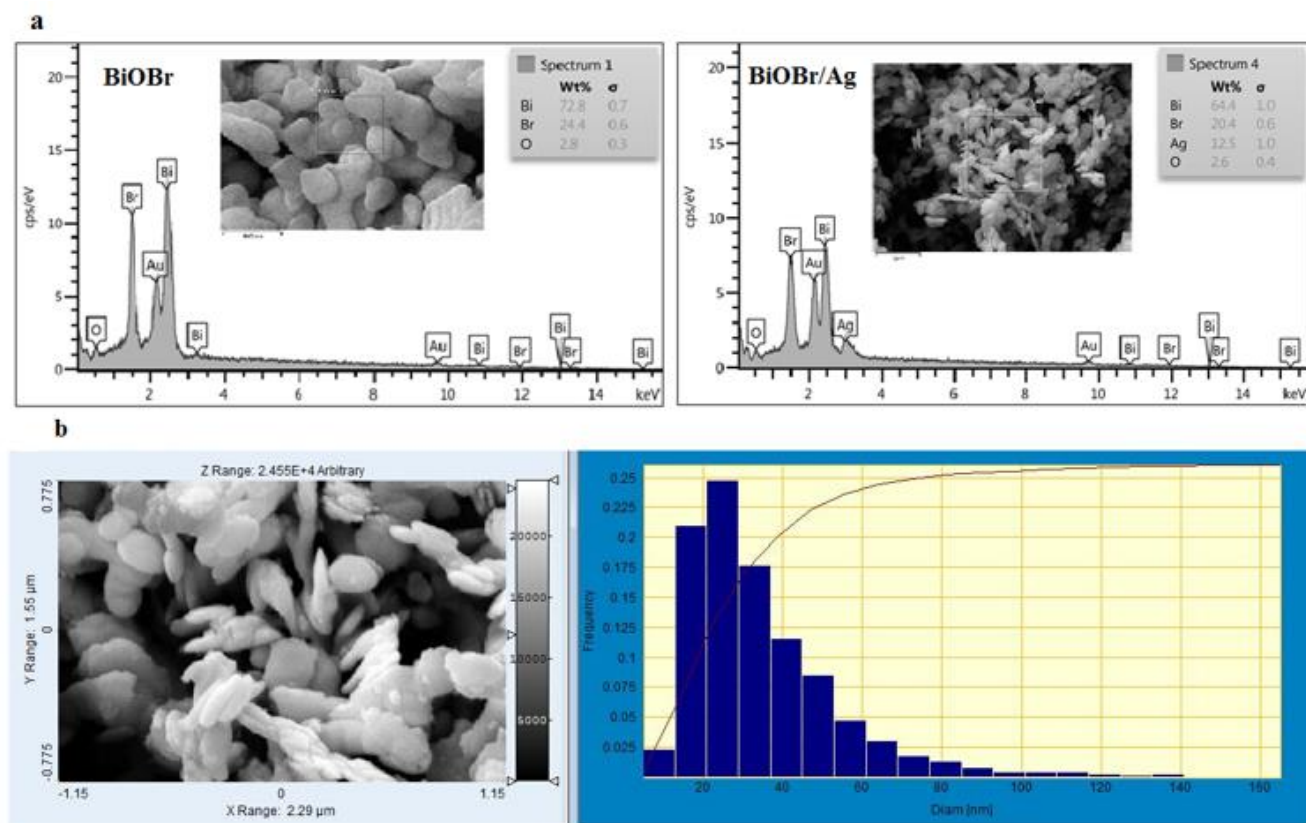
Fig. 5. a) EDX spectra for samples and b) Histogram from SEM BiOBr/Ag nanocomposite.

3.1.5. Raman Spectra

The Raman spectra for the catalyst BiOBr and the composite catalyst BiOBr/Ag are shown in **Fig. 6**. In these spectra, three peaks are observed, where the sharp peak at 126 cm^{-1} is due to the A_1g stretching vibration related to the bond Bi–Br, the peak at 154 cm^{-1} is caused by the Eg stretching vibration for the bond Bi–Br, and the last peak at 370 cm^{-1} is assigned to the vibration of the bond Bi–O in pure BiOBr. The typical peaks for BiOBr/Ag indicate that nanocomposite formation did not affect the BiOBr intrinsic features [29].

As shown in **Fig. 6**, since the amount of Ag NPs loaded on the BiOBr nanoplates is very little, the Raman signals for Ag NPs over the substrate BiOBr are weak, some characteristics of Raman signals are not shown, and also the intensities of the peaks for BiOBr are greatly reduced.
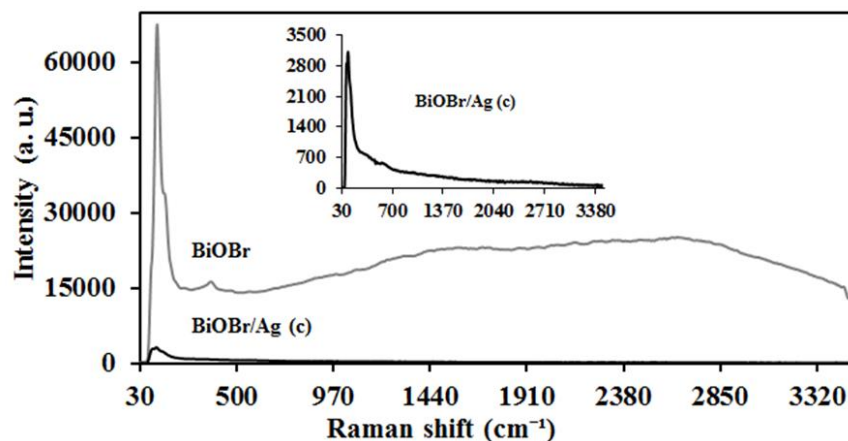
Fig. 6. Raman spectra for BiOBr and BiOBr/Ag (c) nanocomposite.

3.1.6. Photoluminescence (PL) Spectra

The PL spectra in **Fig. 7** show that the understudied samples have clear emission peaks located at around 435-529 nm and 625 nm with the excitation wavelength of 200 nm. The PL spectra were taken to examine the e^--h^+ recombination of the BiOBr nanoplates and Ag NPs. The powerful recombination of e^--h^+ pairs is generally associated with high intensity of fluorescence and low activity of photocatalyst [30]. As shown in Fig. 7, the emission intensities for pure BiOBr are the highest and the PL peak intensities are decreased with Ag loading. The PL spectra suggest that the photo-generated electrons of the BiOBr nanoplates can be efficiently trapped by Ag NPs. This may be an explanation for the higher photocatalytic activity of the BiOBr/Ag nanocomposite compared with that of BiOBr [31, 32].
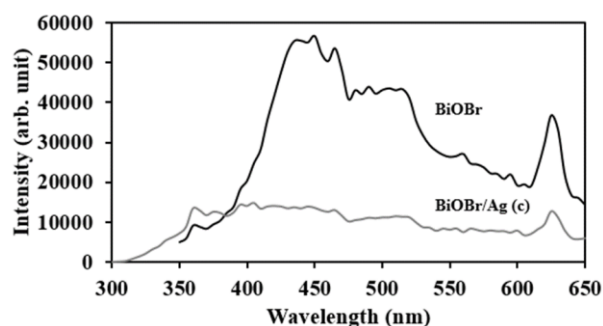
Fig. 7. PL spectra for BiOBr and BiOBr/Ag (c) nanocomposite with an excitation wavelength of 200 nm.

3.2. Photocatalytic Activities Investigation

3.2.1. Photodegradation of MO, DCP, and RhB

The as-prepared photocatalysts were assessed in terms of photocatalytic efficiency through RhB, DCP, and MO degradation under irradiation of LED. According to the results obtained, BiOBr/Ag (c) showed stable performance with excellent properties (**Figs. 8a** and **8c**). The results obtained from photocatalytic studies are shown in Fig. 8. In all cases, the best degradation rate was close to 60-80% after 240 min of irradiation. Providing identical conditions to make a comparable measurement, there was insignificantly direct photolysis of pure MO under LED irradiation. In the photodegradation of MO, after 240 min of irradiation, we observed that Ag grew on the surface of BiOBr, showing much better degradation efficiency than BiOBr. At the end of the degradation, a combination in which the silver concentration was 0.2 M (BiOBr/Ag (c)) yielded the best result (about 63%). Meanwhile, the BiOBr/Ag (a) and BiOBr/Ag (b) nanocomposites

destructed 48% and 42% of MO in 240 min, respectively. Compared to the BiOBr nanoplates, the BiOBr/Ag nanocomposites showed higher MO photodegradation efficiency. Among the synthesized nanocomposites, the BiOBr/Ag (c) exhibited the highest photoactivity. According to the results of photodegradation, the photoactivity of BiOBr/Ag (c) was about one-and-a-half times higher than that of the BiOBr nanoplates.

Besides, DCP and RhB were also employed at a concentration of $10 \ mg \ L^{-1}$ to examine the photocatalytic activity of the BiOBr/Ag (c) nanocomposite. **Figs. 8d** and **8e** show the efficiency of the photocatalysts of BiOBr and BiOBr/Ag (c) for degradation of DCP and RhB under the irradiation of LED. The high photocatalytic proactivity of BiOBr/Ag can be attributed to several factors including the ability of photocatalyst to absorb the molecules of pollutant, its potential for photo-absorption under the visible light, transportability and capability of electron- whole pairs to be separated.

Experiments on the photodegradation of RhB and DCP indicated low degradation of RhB and DCP molecules in the absence of photocatalyst. The BiOBr/Ag (c) nanocomposite was found to destroy 62% and 76% of DCP and RhB in 240 min, respectively. The photoactivity of the nanocomposite BiOBr/Ag (c) was higher than that of the pure BiOBr. The Ag NPs presence in the BiOBr acts as a barrier to the e^--h^+ recombination under the LED irradiation, thereby improving the photoactivity.

As shown in **Fig. 8f**, the MO photodegradation kinetics of various photocatalysts was also investigated. If the photodegradation of MO is considered as a pseudo-first-order reaction; its photocatalytic reaction kinetics can be expressed as follows:

$$\ln(C_0/C) = kt + A,$$

where and k is the rate of apparent photodegradation reaction per minute, t denotes the reaction time, and C_0/C expresses the normalized MO concentration. The k value for pure BiOBr is lower than all the BiOBr/Ag nanocomposites. The highest catalytic activity belongs to the BiOBr/Ag (c) sample ($k = 0.003 \ min^{-1}$), more than twice that of BiOBr nanoplate ($k = 0.0013 \ min^{-1}$). The DCP and RhB photodegradation curves in the form of ln (C_0/C) are shown as a function of time in **Fig. 8g**. The linear fitting for BiOBr/Ag (c) is used to obtain k, pseudo-first-rate kinetic constant [33, 20].
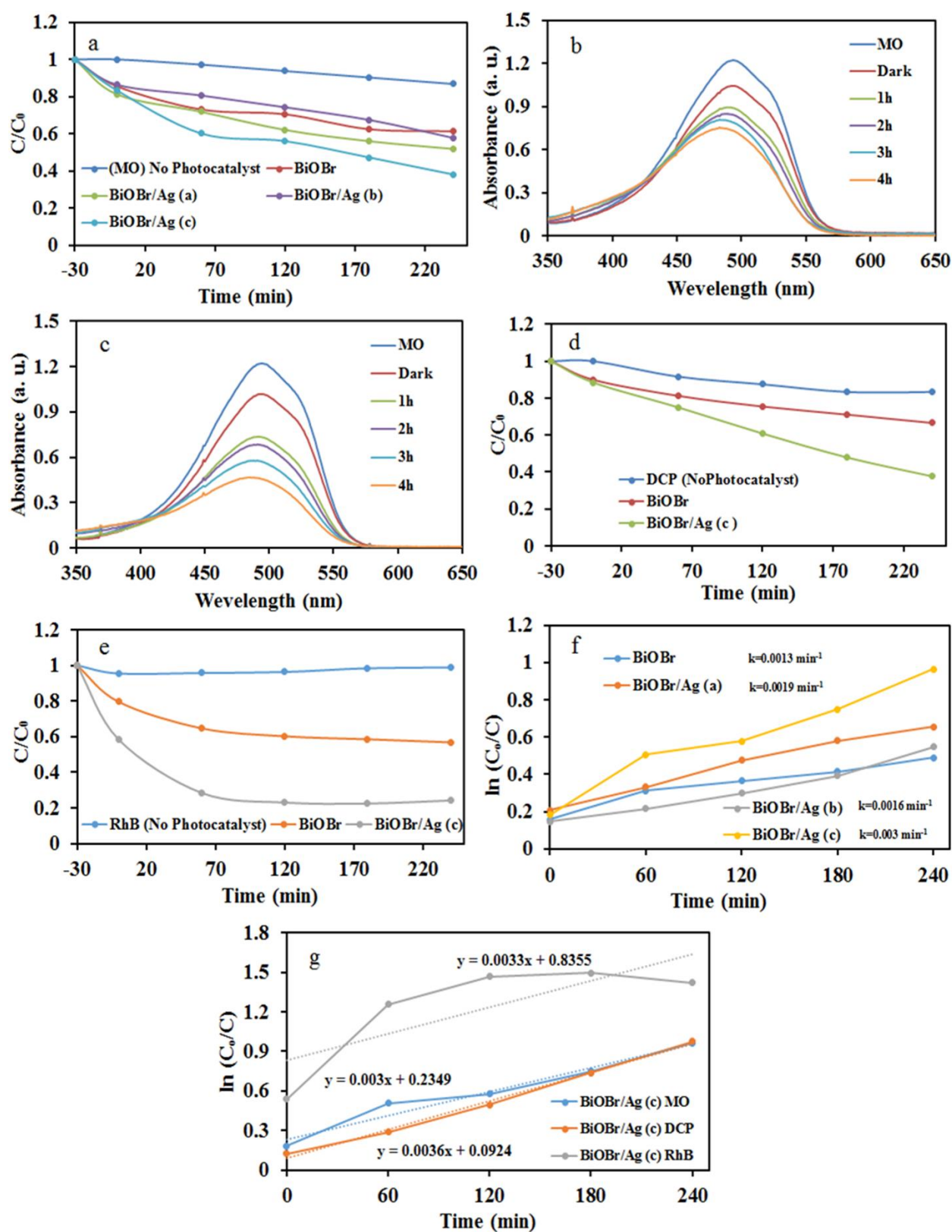
Fig. 8. a) Photodegradation of MO over the prepared samples, curve of absorption versus wavelength for photodegradation of MO b) BiOBr nanoplates and c) BiOBr/Ag (c) nanocomposite, photodegradation of d) DCP and e) RhB over the BiOBr and BiOBr/Ag (c) nanocomposite, f) Kinetics of MO decolorization over the prepared samples, and g) Kinetics of MO, RhB and DCP degradation under the visible light irradiation.

3.2.2. Photocatalytic Mechanism

Some scavengers were chosen including 2 mmol NH₄OX as a hole (h⁺) scavenger, 2 mmol AgNO₃ as an electron scavenger, and 1 mmol *tert*-BuOH as an OH radical scavenger under N₂ saturation condition (O₂ absence) to study the superoxide generation of anion radicals ($^\bullet O_2^-$) in the BiOBr/Ag photocatalytic mechanism. As can be seen in **Fig. 9**, NH₄OX inhibited the photocatalytic activity of BiOBr/Ag. Observation of the highest photocatalytic degradation by BiOBr/Ag reveals that the major species involved in photocatalytic process and the active species involved in photocatalytic reaction are the holes.
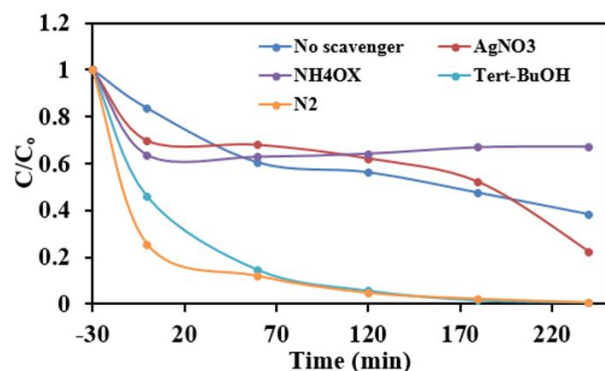

Fig. 9. Photocatalytic mechanism of the BiOBr/Ag nanocomposite in the presence of different scavengers.

3.2.3. Possible Photocatalytic Mechanism

Based on the experimental results, a probable mechanism was suggested for the visible light photocatalytic activity enhancement and charge transfer increase of BiOBr/Ag, as illustrated in **Fig. 10**. The UV–visible diffusive reflectance spectra showed that BiOBr/Ag had a stronger light absorption than absolute BiOBr and can be readily excited under irradiation of LED. Thus, an effective h⁺ could be produced at VB owing to the easy excitation of electrons in BiOBr from VB (3.078 eV) to CB (0.278 eV) under irradiation of LED. This recombination was prevented by the reaction between photo-generated electrons and molecular oxygen (O_2) present in the environment to form $^\bullet O_2^-$, which leads to the degradation of the pollutant. As shown in the PL spectra, the emission intensity of absolute BiOBr nanoplate is the highest, and the peak intensities are decreased with Ag loading. The PL spectra suggest that the BiOBr photo-generated electrons can be efficiently trapped by Ag NPs. Accordingly, in the BiOBr/Ag nanocomposite, the transfer charge was improved, preventing recombination of the electrons and holes. Also, the electrons present in Ag NPs react with O_2 present in the

environment to produce $^\bullet O_2^-$. Furthermore, the photo-generated holes on the surface of BiOBr react with the H_2O molecules present in the environment to produce OH radicals and cause degradation of the pollutant.

There are different values of E° reported for O_2 reduction to superoxide radicals. The reported values are conditional to the solution pH. This study's experiments were conducted at pH of 3 for the selected value of -0.33 V. Accordingly, the CB accumulated electrons are appropriate active species to produce the $^\bullet O_2^-$ (reduction of O_2). The holes in the energy level VB are typically active sites for the OH radical production. The photo-generated holes play a more significant oxidizing agent role in degradation of MO. As mentioned in the study of photocatalytic mechanism, the photo-generated holes perform the central role in photodegradation of MO [34-37].
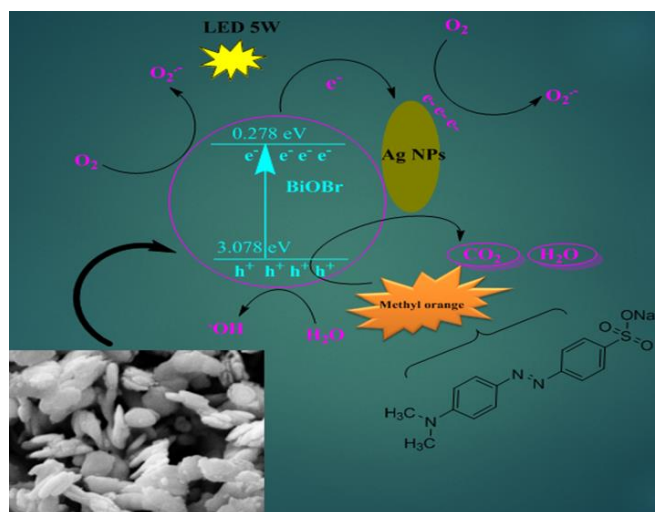
Fig. 10. Schematic representation of the charge transfer in the BiOBr/Ag nanocomposite degradation.

3.2.4. Photocatalyst Reuse

As shown in **Fig. 11**, BiOBr/Ag nanocomposite was gathered and retested in a new cycle to evaluate its performance on MO photodegradation. In the second test, there was a lower rate of MO degradation resulting from reduced amount of recovered photocatalyst. The photocatalytic activity of BiOBr/Ag decreased by only a small amount (less than 6%) after three rounds of recycling.

3.2.5. Comparison with Other Studies

Jiang *et al*. synthesized the BiOBr photocatalysts with Ti doping and Ag decorating by the chemical reduction, photo-reduction, and thermal reduction methods and found that it had a highly efficient photocatalytic activity in destroying the RhB dye. The photodegradation experiments were conducted under

the irradiation of visible light with a daylight 11-W source lamp. The photocatalytic activity of T−Ag samples was closely relative to the content of Ag, as the T−3% Ag photocatalytic activity was the highest in the optimum content of Ag [38]. Yu *et al*. prepared the photocatalyst Ag/BiOBr by a solution combination with photo-deposited method. The photocatalytic reaction tests were performed for the degradation of the dyes Acid orange II (AO), RhB, and MO under the irradiation of 300-W tungsten source lamp [39]. Di et al. adopted the simple approach of ionic liquid-assisted solvothermal to Ag QDs/BiOBr preparation. Under the irradiation of 300-W Xe lamp, the antibiotic agents of ciprofloxacin (CIP), RhB, and tetracycline hydrochloride (TC) were degraded to evaluate the photocatalytic activity of the prepared samples [40]. Guo group reported that the Ag/CDots/BiOBr photocatalyst caused an improvement in the BiOBr photocatalytic activity. The photocatalytic activities of the Ag/CDots/BiOBr were investigated by the photodegradation of 4-chlorophenol, with a 150-W Xe lamp as its irradiation source [41]. Whereas, a facile co-precipitation method was used to synthesize the BiOBr/Ag nanocomposite in this research. Furthermore, to simulate sunlight, the lamp used in this photocatalytic process was white light power down (5-W LED), used less in previous studies. According to the obtained results, the photo-generated loads exhibited a higher performance in separation by using BiOBr/Ag nanocomposite. The photocatalytic mechanism of the used nanocomposite was also studied, in which the created holes had an important role in the process. The results obtained from the comparison of studies can be seen in **Table 4**.
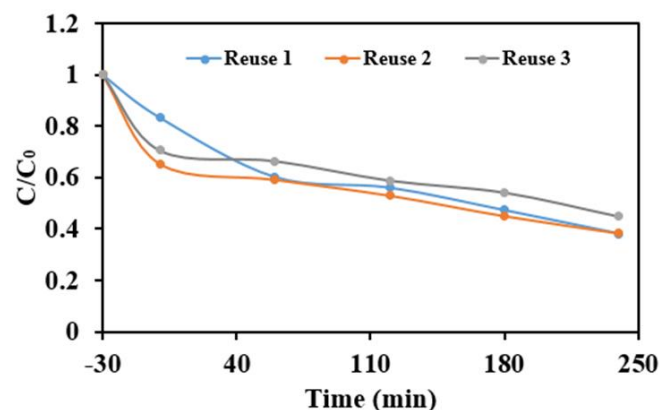
Fig. 11. Recycling tests for photodegrading of MO using the BiOBr/Ag (c) nanocomposite.

Table 4. Comparison of this research with other studies.

Ref.	Photocatalyst	Organic pollutants	Visible light source
[38]	Ag/Ti-dope/BiOBr	RhB	11-W daylight lamp
[39]	Ag/BiOBr	AO, RhB, MO	300-W tungsten lamp
[40]	Ag QDs/BiOBr	CIP, TC, RhB	300-W Xe arc lamp
[41]	Ag/CDots/BiOBr	4-CP	150-W Xe lamp
Present research work	BiOBr/Ag	RhB, DCP, MO	5-W LED (like sunlight)

4. Conclusions

In the present work, the uniform BiOBr/Ag nanocomposite was fully prepared via a facile and subsequently, a reduction method. We demonstrated the synthesis of Ag NPs by the solution-phase chemical reduction of $AgNO_3$ by $NaBH_4$ in the presence of BiOBr. The BiOBr/Ag nanocomposite exhibited a rather high absorption in the visible light region, playing an important role in the photocatalytic reaction. The as-prepared BiOBr/Ag nanocomposite showed a better proactivity than pure BiOBr in organic pollutant degradation, synergizing the effects of BiOBr photocatalyst and nano-sized plasmonic Ag. The findings suggested that more than 76% of RhB was photodegraded under the visible irradiation. The photocatalytic process showed that most of MO photodegradation was carried out via the mechanism of holes. It can be concluded that a good photocatalytic activity was dependent on Ag NPs. Moreover, h^+ was determined as the main active species accountable for MO photodegradation. Those ways of removing pollutants that are cost-effective and easy to use are more appropriate for environmental purification. Therefore, the semi-conductors by doping transition metal can be used to remove organic and inorganic components from water and air because of their attractive properties, for example, high activity, non-toxicity, and low cost. Compounds containing Ag NPs can also be used as antibacterial substances to purify drinking water as well as industrial wastewater by removing organic pollutants.

Acknowledgements

References

[1] Y. Zhou, J. Lu, Y. Zhou, Y. Liu, Environ. Pollut. 252 (2019) 352-365.

[2] E.N. Zare, A. Motahari, M. Sillanpää, Environ. Res. 162 (2018) 173-195.

[3] L. Ye, Y. Su, X. Jin, H. Xie, C. Zhang, Environ. Sci.: Nano. 1 (2014) 90-112.

[4] N. Assi, P.A. Azar, M.S. Tehrani, S.W. Husain, J. Iran. Chem. Soc. 13(9) (2016) 1593-1602.

[5] H. R. Pouretedal, A. M. Sohrabi, J. Iran. Chem. Soc. 13(1) (2016) 73-79.

[6] Y. Mi, M. Zhou, L. Wen, H. Zhao, Y. Lei, Dalton Trans. 43 (2014) 9549-9556.

[7] X. Cao, Z. Lu, L. Zhu, L. Yang, L. Gu, L. Cai, J. Chen, Nanoscale. 6 (2014) 1434-1444.

[8] H. Zhang, Y. Yang, Z. Zhou, Y. Zhao, L. Liu, J. Phys. Chem. C. 118 (2014) 14662-14669.

[9] Z. Jiang, B. Huang, Z. Lou, Z. Wang, X. Meng, Y. Liu, X. Qin, X. Zhang, Y. Dai, Dalton Trans. 43 (2014) 8170-8173.

[10] C. Bi, J. Cao, H. Lin, Y. Wang, S. Chen, RSC Adv. 6 (2016) 15525-15534.

[11] M. Zahedifar, M. Shirani, A. Akbari, N. Seyedi, Cellulose. 26(11) (2019) 6797-6812.

[12] Q. T. H. Ta, S. Park, J. S. Noh, J. Colloid Interface Sci. 505 (2017) 437-444.

[13] S. Naghizadeh-Alamdari, A. Habibi-Yangjeh, M. Pirhashemi, Appl. Surf. Sci. 40 (2015) 111-120.

[14] J. Manna, T. P. Vinod, K. Flomin, R. Jelinek, J. Colloid Interface Sci. 460 (2015) 113-118.

[15] J. Lv, Q. Zhu, Z. Zeng, M. Zhang, J. Yang, M. Zhao, W. Wang, Y. Cheng, G. He, Z. Sun, J. Phys. Chem. Solids. 111 (2017) 104-109.

[16] X. F. Zhang, Z. G. Liu, W. Shen, S. Gurunathan, Int. J. Mol. Sci. 17 (2016) 1534-1567.

[17] S. Gurunathan, J.H. Park, J.W. Han, J. Kim, H. Int. J. Nanomed. 10 (2015) 4203-4223.

[18] W. R. Li, X.B. Xie, Q. S. Shi, H. Y. Zeng, O. Y. You-Sheng, Y.B. Chen, Appl. Microbial. biotechnol. 85 (2010) 1115-1122.

[19] X. Zhu, X. Liang, P. Wang, Y. Dai, B. Huang, Appl. Surf. Sci. 456 (2018) 493-500.

[20] Y. C. Yao, X. R. Dai, X. Y. Hu, S. Z. Huang, Z. Jin, Appl. Surf. Sci. 387 (2016) 469-476.

[21] M. Yaghoubi-berijani, B. Bahramian, S. Zargari, Res. Chem. Intermed. 46 (2020) 197–213.

[22] R. Saraf, C. Shivakumara, S. Behera, N. Dhananjaya, H. Nagabhushana, RSC Adv. 5 (2015) 9241-9254.

[23] A. Esmaeili, M. H. Entezari, RSC Adv. 5 (2015) 97027-97035.

[24] L. Zhang, Z. Wu, L. Chen, L. Zhang, X. Li, H. Xu, H. Wang, G. Zhu, Solid State Sci. 52 (2016) 42-48.

[25] J. Cao, B. Xu, H. Lin, B. Luo, S. Chen, Chem. Eng. J. 185 (2012) 91-99.

[26] S. Yao, R. Zheng, R. Li, Y. Chen, X. Zhou, J. Luo, J. Taiwan Inst. chem. Eng. 100 (2019) 186-193.

[27] Y. T. Prabhu, K. V. Rao, V. S. S. Kumar, B. S. Kumari, World J. Nano Sci. Eng. 4 (2014) 21-28.

[28] A. B. Andrade, N. S. Ferreira, M. E. Valerio, RSC Adv. 7(43) (2017) 26839-26848.

[29] H. Cui, Y. Zhou, J. Mei, Z. Li, S. Xu, C. Yao, J. Phys. Chem. Solids. 112 (2018) 80-87.

[30] H. Zhang, C.G. Niu, S.F. Yang, G.M. Zeng, RSC Adv. 6 (2016) 64617-64625.

[31] S. Hu, L. Jiang, Y. Tu, Y. Cui, B. Wang, Y. Ma, Y. Zhang, J. Taiwan Inst. Chem. Engrs. 86 (2018) 113-119.

[32] S. Lee, Y. Park, D. Pradhan, Y. Sohn, J. Ind. Eng. chem. 35 (2016) 231-252.

[33] H. Liu, Y. Hu, Z. Zhang, X. Liu, H. Jia, B. Xu, Appl. Surf. Sci. 355 (2015) 644-652.

[34] B.H. Bielski, D.E. Cabelli, Active oxygen in chemistry. Springer, Dordrecht (1995) 66-104.

[35] N. Omrani, A. Nezamzadeh-Ejhieh, Sep. Purif. Technol. 235 (2020) 116228-116232.

[36] C. Chen, W. Ma, J. Zhao, Chem. Soc. Rev. 39(11) (2010) 4206-4219.

[37] M. Babaahamdi-Milani, A. Nezamzadeh-Ejhieh, J. Hazard. Mater. 318 (2016) 291-301.

[38] G. Jiang, R. Wang, X. Wang, X. Xi, R. Hu, Y. Zhou, S. Wang, T. Wang, W. Chen, ACS Appl. Mater. Interfaces. 4(9) (2012) 4440-4444.

[39] C. Yu, C. Fan, X. Meng, K. Yang, F. Cao, X. Li, React. Kinet. Mech. Catal. 103 (2011) 141-151.

[40] J. Di, J. Xia, M. Ji, B. Wang, S. Yin, Y. Huang, Z. Chen, H. Li, Appl. Catal. B Environ. 188 (2016) 376-387.

[41] Y. Guo, J. Zhang, D. Zhou, S. Dong, J. Mol. Liq. 262 (2018) 194-203.